



## RESEARCH ARTICLE

10.1002/2015JC011071

## Key Points:

- Internal seiche propagation caused by bottom boundary layer conversion of seiche energy to turbulence
- High (water velocity)/(vertical propagation speed) ratio associated with net vertical propagation
- Stratification inhibited turbulence measured within 0.4 m of lakebed

## Correspondence to:

S. M. Henderson,  
steve\_henderson@wsu.edu

## Citation:

Henderson, S. M. (2016), Turbulent production in an internal wave bottom boundary layer maintained by a vertically propagating seiche, *J. Geophys. Res. Oceans*, 121, doi:10.1002/2015JC011071.

Received 23 JUN 2015

Accepted 6 MAR 2016

Accepted article online 11 MAR 2016

## Turbulent production in an internal wave bottom boundary layer maintained by a vertically propagating seiche

Stephen M. Henderson<sup>1</sup>
<sup>1</sup>School of the Environment, Washington State University Vancouver, Vancouver, Washington, USA

**Abstract** Internal seiches, which supply the energy responsible for mixing many lakes, are often modeled as vertically standing waves. However, recent observations of vertical seiche propagation in a small lake are inconsistent with the standard, vertically standing model. To examine the processes responsible for such propagation, drag and turbulent production in the bottom boundary layer of a small lake are related to the energy supplied by a propagating seiche (period 10–24 h). Despite complex and fluctuating stratification, which often inhibited mixing within 0.4 m of the bed, bottom stress was well represented by a simple drag coefficient model (drag coefficient  $1.5 \times 10^{-3}$ ). The net supply of seiche energy to the boundary layer was estimated by fitting a model for internal wave vertical propagation to velocity profiles measured above the boundary layer (1–4.5 m above lakebed). Fitted reflection coefficients ranged from 0.3 at 1 cycle/d frequency to 0.7 at 2.4 cycles/d (cf. near-unity coefficients of classical seiche theories). The net supply of seiche energy approximately balanced boundary layer turbulent production. Three of four peaks in production and energy flux occurred 0.8–2.2 days after strong oscillating winds, a delay comparable to the time required for seiche energy to propagate to the lakebed. A model based on the estimated drag coefficient predicted the observed frequency dependence of the seiche reflection coefficient. For flat-bed regions in narrow lakes, the model predicts that reflection is controlled by the ratio of water velocity to vertical wave propagation speed, with sufficiently large ratios leading to weak reflection, and clear vertical seiche propagation.

## 1. Introduction

Internal waves play an important role in the mixing of stratified lakes and oceans. In many lakes, water flows are dominated by basin-wide internal waves called seiches [Mortimer, 1952]. Seiche energy is often generated by fluctuating winds, and removed by conversion to turbulent energy. Sometimes, seiche energy can be transferred to smaller scales by conservative nonlinear wave interactions before being lost to turbulence [Horn *et al.*, 2001; de la Fuente *et al.*, 2010]. The conversion of internal wave energy to turbulence (hereafter “turbulent production”) sustains turbulent mixing of heat [Lorrai *et al.*, 2011], sediments [Pierson and Weyhenmeyer, 1994], chemicals [MacIntyre and Jellison, 2001], organisms [Serra *et al.*, 2007], and pollutants [Sorensen *et al.*, 2004].

Turbulent production and mixing may be intensified in internal wave bottom boundary layers (BBLs). Although BBLs are thin, near-bed turbulence is so intensified that, in lakes, BBLs are responsible for much of the lake-wide loss of internal wave energy [Wüest *et al.*, 2000]. BBLs may be responsible for much of the vertical mixing of density, nutrients, and pollutants in lakes [Goudsmit *et al.*, 1997; Wüest and Lorke, 2003] and may also play an important role in the vertical mixing of some estuaries [Inall, 2009]. Further interest in internal wave BBLs is motivated by their influence on sediment transport [Pierson and Weyhenmeyer, 1994] and sediment-water biogeochemical fluxes [Lorke *et al.*, 2003; Holtappels *et al.*, 2011; Deemer *et al.*, 2015].

In small lakes, internal seiches are usually viewed as standing waves (progressive Kelvin waves, which can propagate horizontally around the edge of larger lakes [Atenucci *et al.*, 2000], are neglected here). In theory, standing patterns result if internal waves are reflected perfectly from horizontal and vertical basin boundaries. However, loss of wave energy to BBL turbulent production could lead to incomplete wave reflection from the bed, and net vertical propagation. Weak vertical propagation has been modeled using coupled modes [Brink and Allen, 1978] for rectangular basins [Shimizu and Imberger, 2009]. On the continental shelf, Brink [1988] modeled analogous vertical internal wave propagation. Field observations of seiches have

© 2016. The Authors.

This is an open access article under the terms of the Creative Commons Attribution-NonCommercial-NoDerivs License, which permits use and distribution in any medium, provided the original work is properly cited, the use is non-commercial and no modifications or adaptations are made.

usually been compared with vertically standing models [e.g., LaZerte, 1980; Münnich *et al.*, 1992; Pannard *et al.*, 2011], but in a small lake, Henderson and Deemer [2012] observed vertical seiche propagation. Vertical propagation aside, the waves observed by Henderson and Deemer [2012] resembled standard seiches: they were likely generated by winds, with a standing-wave pattern in the horizontal and a horizontal wavelength about twice the lake length. Reexamination of published observations reveals other cases of vertical propagation [e.g., Serra *et al.*, 2007, Figure 8; LaZerte, 1980, Figures 6 and 8; Vidal *et al.*, 2008, Figures 5 and 8]. Therefore, vertical seiche propagation might not be uncommon. In all cases listed above, the patterns of seiche velocity (and temperature) fluctuations propagated upward. A property of internal waves is that such upward “phase propagation” implies downward energy propagation [Phillips, 1977], consistent with BBL absorption of wave energy by turbulent production [Henderson and Deemer, 2012]. Therefore, propagating seiches carry energy to the BBL, potentially sustaining turbulent production and mixing. Measured turbulent production within the BBL has not previously been compared with the energy supplied by vertical seiche propagation.

This manuscript aims to clarify the relationship between vertical seiche propagation and BBL turbulent production using field observations and a simple BBL energy balance:

$$F_I - F_R = D, \quad (1)$$

where  $F_I$  and  $F_R$  are, respectively, the energy fluxes carried to and from the BBL by incident and reflected internal waves, and  $D$  is the loss of wave energy in the BBL. Within-BBL conservative nonlinear transfers of seiche energy to smaller-scale motions will be neglected, so  $D$  is assumed to equal turbulent production. This assumption, theoretically justified for cases where seiche amplitude is much less than water depth [Horn *et al.*, 2001], will be tested by comparing direct measurements of turbulent production with estimates of the energy flux  $F_I - F_R$ . Observations are contrasted with the vertically standing prediction ( $F_I = F_R$ ) of the standard vertically standing seiche model, which results from neglect of  $D$ . Using (1) and a simple parameterization for  $D$ , a model for incomplete internal wave reflection is developed to explain seiche propagation.

The field site and instrumentation are introduced in section 2. In the small lake where temperature and turbulent velocity were measured, flows were dominated by vertically propagating internal seiches with 0.4–1 day period. Next (section 3), measured vertical and temporal variability of velocity, turbulent Reynolds stress, and stratification are described. Within the approximately 1 m thick BBL, turbulence was strongly time dependent and often inhibited by stratification.

As a step toward explaining seiche propagation, models for bottom drag and turbulent production (i.e.,  $D$  in (1)) were calibrated using observations of near-bed velocity and turbulent stress (section 4). Seiche propagation was then quantified using velocities measured just above the BBL (section 5). Using a simple wave propagation model, energy fluxes  $F_I$  and  $F_R$  were estimated by fitting the amplitudes of incident and reflected internal waves to above-BBL velocity profiles. The ratio between reflected and incident wave amplitudes, called the reflection coefficient and denoted  $R$ , was evaluated as a function of frequency and compared with the  $R = 1$  value associated with vertically standing waves. Turbulent production and wave propagation are compared in section 6. By combining (1) with the turbulent production models developed in section 4, a model predicting the reflection coefficient was derived, and tested against observed reflection coefficients. Finally, results are summarized (section 7). Using the model developed in section 6, the physical explanation of seiche propagation is discussed. Potential for the model to predict departures from classical seiche theory in other lakes is outlined, together with possible limitations.

## 2. Field Site and Instrumentation

Water velocity and temperature were measured in Lacamas Lake, Washington (Figure 1) from 19 May to 17 June 2011. Velocities in this lake are dominated by fluctuations of a few cm/s, with periods in the range 0.4–1 day. These fluctuations result from a vertically propagating internal seiche, with upward phase propagation, horizontal wavelength about twice the lake length, and vertical wavelength less than the lake depth [Henderson and Deemer, 2012]. Outside the BBL, velocities were predominantly directed along the long axis of the narrow lake. The force required to prevent Coriolis from deflecting the along-lake flows into the across-lake direction is provided by across-lake baroclinic pressure gradients (i.e., an approximate across-lake thermal wind balance is observed [Henderson and Deemer, 2012]). Near the center of the lake, where

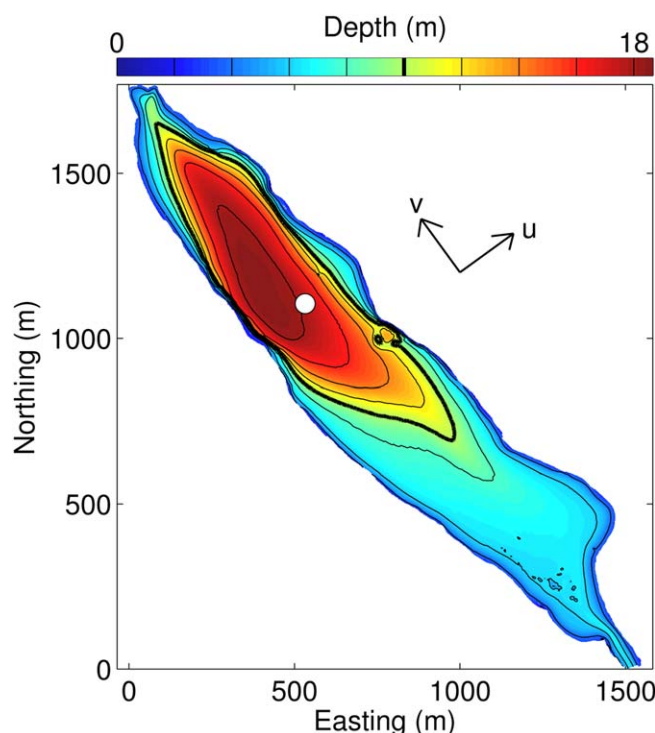


**Figure 1.** Lacamas Lake bathymetry and location of tripod (circle, location 45.61983°N 122.43015°W). Arrows show direction of across-lake velocity  $u$  and along-lake velocity  $v$ . Northing and Easting measured from 45.60977°N, 122.43667°W.

measurements were made, the internal seiche likely resembles a pair of internal Kelvin waves, one propagating along each shore, and both propagating vertically. Theoretically, the two Kelvin waves give a  $\cosh(x/L_R)$  dependence of velocity on across-lake position  $x$  (with  $x = 0$  at the lake's midpoint), where the internal Rossby Radius  $L_R$  proves to be about 210 m (section 5). This across-lake dependence of velocity will be neglected in analysis below, which will treat velocity as independent of  $x$ . Kelvin wave theory predicts that errors associated with this approximation do not exceed 27% (for the depths exceeding 14 m, considered below, the lake width does not exceed about 300 m, so  $-150 \text{ m} < x < 150 \text{ m}$ , and  $\cosh(x/L_R)$  ranges between 1 and 1.27).

Surface waves likely had little effect on BBL flows. Visual observations indicated that dominant surface wave lengths were less than 5 m, and velocities associated with such short waves are strongly attenuated with depth (by

linear theory, velocities at 17.5 m depth are less than near-surface velocities by a factor of  $\cosh[(2\pi/5 \text{ m}) \times 17.5 \text{ m}] = 1.8 \times 10^9$  [Phillips, 1977]).

Velocity was measured using three 2 MHz Nortek Aquadopp Acoustic Doppler Profilers (ADPs) mounted on an aluminum tripod. The tripod was deployed on the lakebed in about 17.5 m depth, about 100 m south-east of the lake's deepest point (Figure 1). ADPs 1 and 2 were mounted at elevation  $z \approx 1.3 \text{ m}$  above the bed, pointed downward to measure velocity every 0.015 m from  $z = 0.15 \text{ m}$  to  $z = 1.14 \text{ m}$  (Figure 2). At  $z < 0.15 \text{ m}$ , velocities may have been contaminated by acoustic sidelobe reflections from the bed, and were neglected. ADP 3 was mounted at  $z \approx 1.6 \text{ m}$ , pointed upward to measure velocity every 0.023 m from  $z = 1.8 \text{ m}$  to  $z = 4.7 \text{ m}$ . Before deployment, a spirit level was used to align the instruments with the tripod. All ADPs operated in pulse-coherent mode [Lohrmann *et al.*, 1990]. A long (6.8 m) pulse-to-pulse distance yielded high-resolution, low noise measurements; the root-mean-square (rms) noise of 2 Hz measurements from ADPs 1 and 2, estimated from small-scale, high-frequency variance, was slightly less than  $10^{-3} \text{ m s}^{-1}$ . Low ( $< 90\%$ ) correlation data were discarded, and hourly averages of remaining measurements are used for all velocity time series presented below. If correlations were  $< 90\%$  for more than 40% of the velocities measured within an hour (as occurred for 2% of all sampled hours between 19 May to 17 June), all data from that hour were discarded.

Every velocity logged by ADP 1 was obtained by internally averaging measurements over a half-second interval (i.e., the "single-sample duration" was 0.5 s). Continuous bursts of 300 such 0.5 s samples were recorded (i.e., the "burst duration" was 150 s). After each 150 s sampling burst, the instrument rested for 150 s before beginning another 150 s sampling burst (i.e., the "repeat interval," which is the burst duration plus resting time, was 300 s). ADP 3 recorded a single 0.5 s sample every 15 s (i.e., single-sample duration = 0.5 s, burst duration = 0.5 s, and repeat interval = 15 s).

Across-lake and along-lake hourly-mean velocities are denoted  $\bar{u}$  and  $\bar{v}$ . Following Henderson and Deemer [2012], the along-lake direction,  $36^\circ$  counterclockwise from North (Figure 1), was chosen as the principal axis of hourly-mean velocities measured above the BBL. The two downward ADPs were in excellent agreement: at

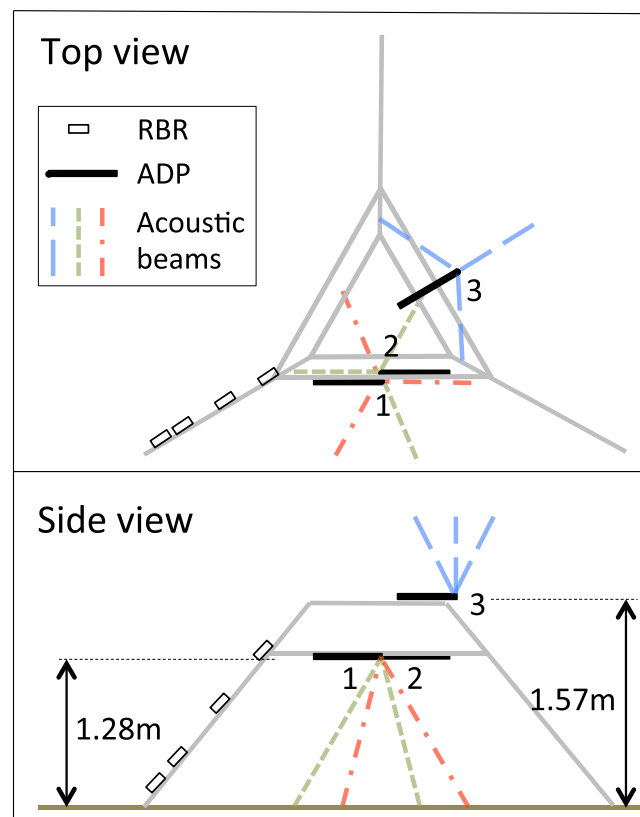


**Figure 2.** Instrument configuration on tripod. Grey lines indicate aluminum tripod, unfilled squares indicate RBR temperature loggers, and black bars indicate ADPs 1–3. Red dot-dashed, green short-dashed, and blue long-dashed lines, respectively, indicate the acoustic beams of ADPs 1, 2, and 3.

every elevation between 0.15 and 0.7 m, linear regression between duplicate hourly-mean velocities from ADPs 1 and 2 yielded  $0.99 < \text{regression slope} < 1.01$ ,  $r^2 > 0.99$ , and offset  $< 2.9 \times 10^{-4} \text{ m s}^{-1}$ .

All velocities presented below were measured by ADPs 1 and 3. ADP 2, which recorded a single 0.5 s sample every 15 s (i.e., single-sample duration = 0.5 s, burst duration = 0.5 s, repeat interval = 15 s), was used only to calculate the Reynolds stress from the measured turbulent velocity. The Reynolds stress ( $\tau_x, \tau_y$ ) =  $\rho(\overline{u'w'}, \overline{v'w'})$  is the vertical (positive upward) transport of horizontal momentum by turbulent eddies [Monin and Yaglom, 1975] (here  $\rho$  is the water density,  $u', v'$  are boundary-parallel turbulent velocities,  $w'$  is the boundary-normal turbulent velocity, and the overbar denotes a 1 h average). For every instrument, acoustic beam, and elevation, turbulent velocities were calculated by subtracting fitted quadratic functions of time from each hourly velocity time series. A method resembling that of Vermeulen et al. [2011] was used to calculate Reynolds stresses by combining

data from the two ADPs. First, following an approach often used to estimate stress from four-beam acoustic current profilers [e.g., Lu and Lueck, 1999], differences between along-beam turbulent velocity variances were used to estimate Reynolds stress components. Across-lake and along-lake Reynolds stresses were then calculated using the redundant data provided by the six acoustic beams of ADPs 1 and 2 (full details in Appendix A). Turbulent production [Monin and Yaglom, 1975] was calculated from estimated mean velocity and Reynolds stress as  $P = -\rho^{-1}(\tau_x \partial \bar{u} / \partial z + \tau_y \partial \bar{v} / \partial z)$  (units  $\text{m}^2 \text{s}^{-3} = \text{W/kg}$ ; vertical derivatives were calculated by finite differencing vertical profiles of hourly-mean velocity).

Temperature was measured using RBR XR-1060 fast-response loggers at  $z = 0.2, 0.4 \text{ m}$  (recording every 2 s), RBR XR-420 CT loggers at  $z = 0.9, 1.4 \text{ m}$  (recording every 6 s), and Onset Hobo Pro V2 loggers at  $z = 1.9, 2.8, 3.9, \text{ and } 4.9 \text{ m}$  (recording every 5 min). All temperatures presented are hourly averages.

During a second deployment, from 15 to 24 July, an Acoustic Doppler Velocimeter (ADV, Nortek Vector) measured 4 Hz time series of three-dimensional velocity at 0.31 m above the bed. Two ADPs were also deployed, in a similar configuration to ADPs 1 and 2 of the 19 May to 17 June deployment. Data from this deployment were used only to compare ADP-based and ADV-based Reynolds stress estimates (fair agreement was found: the dominant EOF between the ADV and ADP complex stresses  $\overline{u'w'} + i \overline{v'w'}$  explained 89% of the stress variance summed over the two estimates, with a best fit rotation error of  $10^\circ$  between instruments, and ADV stress magnitude  $\approx 0.91 \times \text{ADP stress magnitude}$ . Further details are in Appendix A).

Bathymetry was estimated from a multibeam survey conducted in 2014. Data obtained using a 400 kHz, 256-beam echosounder (R2 Sonic 2024) were interpolated onto a regular grid with 1.52 m spacing. Lakebed slopes, estimated by finite differencing bathymetry over 100 m sections centered on the tripod deployment location, were  $1.3^\circ$  in the across-lake direction (up to Northeast) and  $0.24^\circ$  in the along-lake direction (up to Southeast).



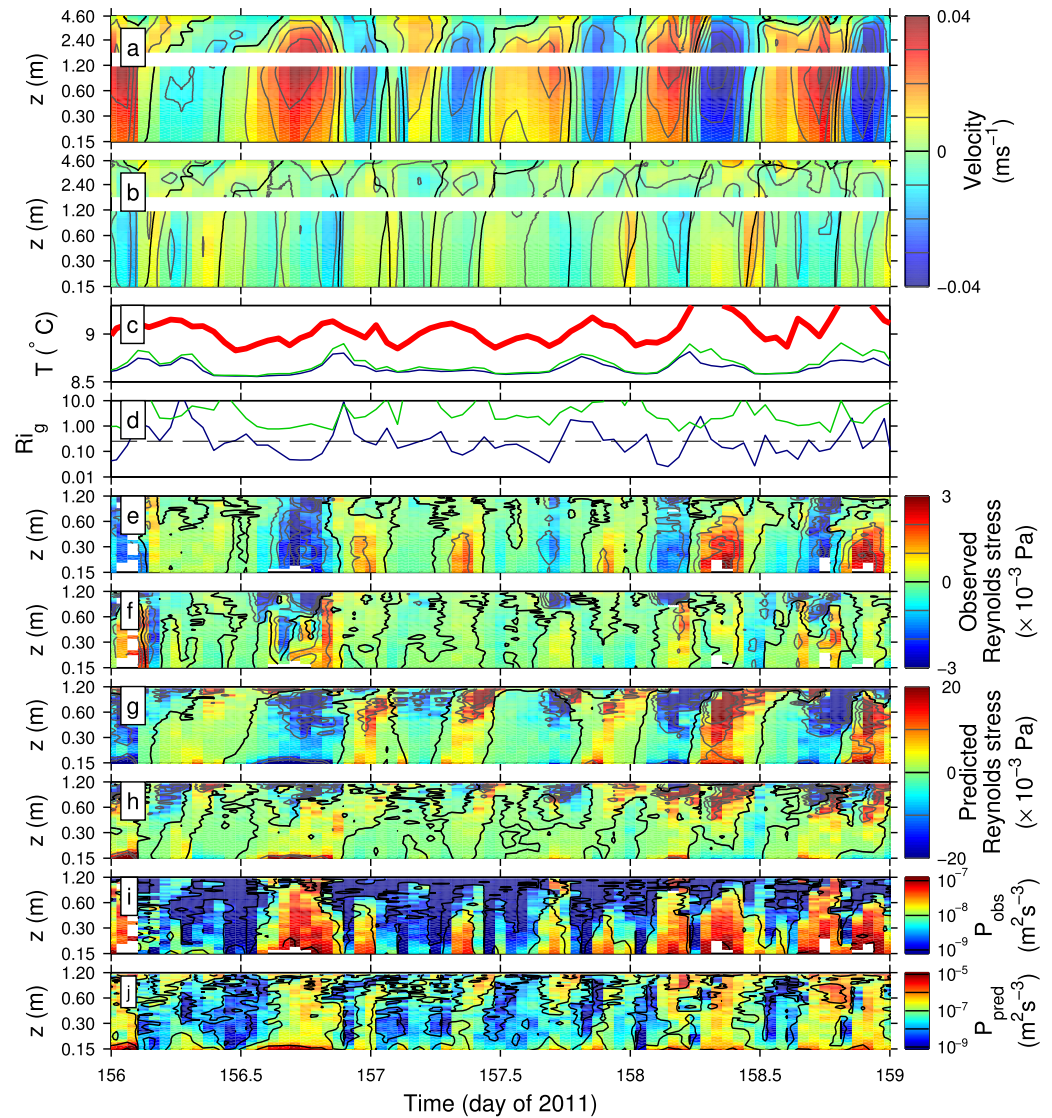


**Figure 3.** Sample time series of hourly data from Deployment 1. (a) Along-lake and (b) across-lake velocities. (c) Temperature at elevations 0.2, 0.9, and 3.9 m (thin dark blue, thin light green, and thick red lines). (d) Richardson number  $Ri$  between 0.2 and 0.9 m (dark blue) and between 0.9 and 3.9 m (light green). Horizontal dashed line marks  $Ri = 0.25$ . (e) along-lake and (f) across-lake observed Reynolds stress. (g) along-lake and (h) across-lake Reynolds stress predicted by mixing-length model. (i) Observed and (j) predicted (from mixing-length model) turbulent shear production.

For both deployments, discrepancies between the two tilts measured by ADPs 1 and 2 were  $<1^\circ$ . The average of the two ADP tilts ( $2^\circ$  and  $1^\circ$ , respectively, for 19 May and 15 July deployments) was comparable to the bed slope estimated from bathymetric surveys. However, errors in ADP tilt measurements are estimated by the manufacturer to be up to  $2^\circ$ . Therefore, errors in measured tilts were likely substantial compared with both the bed slope and the difference between the two ADP tilts.

### 3. Overview of Observations

This section will present a representative 3 day time series of hourly-mean velocity, stratification, turbulent Reynolds stress, and turbulent production (Figure 3), emphasizing the role of stratification in inhibiting BBL turbulence.

Velocity fluctuated through each internal wave period, with along-lake velocity  $v$  dominating over across-lake velocity  $u$  (Figures 3a and 3b). Flow speeds were maximum about 1 m above the bed (Figure 3a), where

the root-mean-square (rms) along-lake velocity reached  $1.6 \times 10^{-2} \text{ m s}^{-1}$ . Nearer the bed, flow speeds declined with decreasing elevation, likely owing to turbulent friction in the BBL. Flow speeds also declined with increasing elevation above  $z = 1 \text{ m}$ , reaching  $9.4 \times 10^{-3} \text{ m s}^{-1}$  rms at  $z = 4 \text{ m}$ . This variability between 1 and 4 m above the bed will be explained in section 5 by examining the nodal structure of partially reflected internal waves.

Temperature fluctuated by about  $0.25\text{--}0.5^\circ\text{C}$  during each internal wave period (Figure 3c). Upslope velocity (positive  $u$ ) was usually associated with decreasing temperature, as colder water was carried up from deeper parts of the lake, whereas downslope velocity was usually associated with increasing temperature (compare Figures 3b and 3c). Clear temperature stratification was observed above the BBL (between  $z = 0.9$  and  $3.9 \text{ m}$ , compare green and red lines in Figure 3c). In contrast, stratification within the BBL (between  $z = 0.2$  and  $0.9 \text{ m}$ , compare blue and green lines, Figure 3c) was intermittent, with the clearest stratification associated with the warmest temperatures. This correlation between strong stratification and warm temperatures is qualitatively consistent with the “Shear-Induced Periodic Stratification” (hereafter SIPS, which is a periodic tilting of isotherms by sheared BBL velocities) noted by previous researchers [Lorke et al., 2005; Becherer and Umlauf, 2011; Lorrai et al., 2011; Umlauf and Burchard, 2011].

Temperature measurements from  $z = 0.4 \text{ m}$  (not shown) show that stratification was more consistently stable in the outer BBL (temperature decreased from  $z = 0.4$  to  $0.9 \text{ m}$  in 96% of cases) than in the inner BBL (temperature decreased from  $z = 0.2$  to  $0.4 \text{ m}$  in 76% of cases). The decline in stable stratification as the bed is approached may result from intensified near-bed mixing. Prolonged temperature time series (not shown) displayed summer warming trends of  $0.83\text{--}1.3 \times 10^{-2} \text{ }^\circ\text{C d}^{-1}$  superposed on the more rapid wave-induced fluctuations.

Owing to the temperature stratification, the potential density, averaged over 19 May to 17 June, declined from  $999.808 \text{ kg m}^{-3}$  at  $z = 0.2 \text{ m}$  to  $999.778 \text{ kg m}^{-3}$  at  $z = 4.9 \text{ m}$  (not shown). The associated mean buoyancy frequency  $N = [-(g/\rho)\partial\rho/\partial z]^{1/2}$  increased from  $7.6 \times 10^{-3} \text{ s}^{-1}$  at  $z = 0.2 \text{ m}$  to  $9.0 \times 10^{-3} \text{ s}^{-1}$  at  $z = 4.6 \text{ m}$  ( $\rho$  = mean density estimated by fitting a smooth curve through the profile of time-averaged density measurements).

Since wave periods were comparable to the inertial period (17 h), theory suggests that along-lake flows persisted sufficiently long to be deflected toward the across-lake direction by Coriolis. Previously, for locations above the BBL, Henderson and Deemer [2012] found that substantial flow deflection was prevented by across-lake tilting of isotherms and resulting baroclinic pressure gradients. Next, for locations within the BBL, it will be shown that major deflection was likely also prevented by baroclinic pressure gradients. First, consider BBL flows above flat beds, for which within-BBL baroclinic forcing may be ignored, and theories for oscillating Ekman layers predict that flow will spiral to the left as the bed is approached [Maas and van Haren, 1987]. Here leftward deflection was observed, but was small; linear regression between the complex velocities  $u + iv$  at elevations 0.15 and 1 m indicates that the 0.15 m velocity was directed  $8^\circ$  to the left of the 1 m velocity ( $r^2 = 0.85$ ). To explain this small deflection, next consider BBL flows over sloping beds, for which within-BBL baroclinic forcing may be substantial. Upslope or downslope BBL flows steadily tilt isotherms, generating buoyancy forces that can bring across-slope flows to a halt over a time of order  $(N\theta)^{-1}$ , which is slightly over an hour in this case (here  $\theta$  is the bed slope). Since this time scale is substantially less than both the inertial period (the slope Burger number  $N\theta/f = 2$ ) and the wave period, buoyancy forces are expected to quickly arrest across-slope flows, likely explaining the dominance of along-lake flows (Brink and Lentz [2010] provide a theoretical discussion of oscillating, slopping BBLs).

The Reynolds number  $|u_1|^2/(2\pi\sigma\nu) \approx 2 \times 10^6$  exceeded the minimum value  $1.6 \times 10^5$  required for turbulence in unstratified oscillatory BBLs [Sleath, 1984] (here  $\nu$  = kinematic viscosity,  $\sigma = 0.7 \text{ day}^{-1}$  is the cyclic wave frequency, and  $|u_1|$  = rms water speed 1 m above the bed). However, stratification often inhibited mixing, as indicated by the Richardson number [Phillips, 1977]

$$Ri = \frac{g(\rho_l - \rho_u)(z_u - z_l)}{\rho_l[(u_l - u_u)^2 + (v_l - v_u)^2]}, \quad (2)$$

where  $\rho_u$ ,  $u_u$ , and  $v_u$  are density, across-lake velocity, and along-lake velocity at elevations  $z_u$ . Above the BBL ( $z_l, z_u = 0.9 \text{ m}, 3.9 \text{ m}$ ),  $Ri$  always exceeded 0.25, indicating strong suppression of mixing by stratification (green curve, Figure 3d). Within the BBL ( $z_l, z_u = 0.2 \text{ m}, 0.9 \text{ m}$ ),  $Ri$  typically oscillated between 0.07 and 0.6, indicating that local stratification periodically inhibited mixing (blue curve, Figure 3d). High  $Ri$  was

associated with temperature maxima, a pattern that is related to the fluctuating temperature stratification discussed above, and that may result from SIPS.

The Reynolds stress [Monin and Yaglom, 1975] is presented in Figures 3e and 3f. The along-lake Reynolds stress  $\tau_y = \rho \overline{v'w'}$  tended to be positive (negative) when the along-lake velocity was negative (positive, compare Figures 3a and 3e). Similarly, the near-bed across-lake Reynolds stress  $\tau_x = \rho \overline{u'w'}$  tended to be positive (negative) when the across-lake velocity was negative (positive, compare Figures 3b and 3f). These trends are expected, as the prevailing momentum is mixed downward before eventually being transferred to the lakebed by bottom friction. Reynolds stress showed a strong depth dependence, with peak magnitudes observed near the bed, often declining to near-zero values within 0.7 m of the bed. Such depth dependence of stress oscillations is characteristic of wave BBLs [Sleath, 1984]. Indeed, the wave BBL could be defined as the region over which wave-frequency Reynolds stress tends to nearly zero. Above 0.7 m elevation, stress estimates became intermittent, with mostly small values punctuated by occasional high-intensity bursts (e.g., days 156.7 and 158.2, Figures 3e and 3f). At these high ( $z > 0.7$  m) elevations, structure functions [Wiles et al., 2006; Lucas et al., 2014] revealed occasional bursts of high-velocity variance at small (0.015–0.045 m) scales (not shown). These observations might indicate flow disturbance by instruments or the tripod, casting doubt on stresses measured above  $z = 0.7$  m.

Turbulent production  $P = -\rho^{-1}(\tau_x \partial \bar{u} / \partial z + \tau_y \partial \bar{v} / \partial z)$  declined rapidly with increasing elevation (Figure 3i). Hourly-mean production was depth averaged over the inner BBL ( $z = 0.2$ – $0.4$  m) and the outer BBL ( $z = 0.4$ – $0.7$  m), and empirical probability distributions were calculated for the two resulting 696 h time series. As expected, most production values were positive (91% and 81% of cases, respectively, for inner and outer BBL), indicating a tendency for turbulence to gain energy from internal waves by mixing momentum down-gradient. The minority of negative values was small in magnitude, and may result from instrument noise, from random fluctuations in turbulent fluxes, or from delayed response of turbulence to time-dependent shear (delays are expected in oscillating BBLs [Lorke et al., 2002]). For the inner BBL, the tenth, fiftieth, and ninetieth percentiles of the probability distribution for production were, respectively,  $1.8 \times 10^{-11}$ ,  $4.8 \times 10^{-9}$ , and  $2.7 \times 10^{-8}$  W kg $^{-1}$  (here the fiftieth percentile is the median). Production tended to be smaller in the outer BBL (for  $z = 0.4$ – $0.9$  m, the tenth, fiftieth, and ninetieth percentiles were  $-6.8 \times 10^{-10}$ ,  $2.7 \times 10^{-9}$ , and  $2.0 \times 10^{-8}$  W kg $^{-1}$ ).

In the absence of stratification and time-varying flow, the vertical scale of near-bed turbulent eddies is about  $\kappa z$ , where  $\kappa = 0.4$  is von Karman's constant. However, the order-one Richardson numbers noted above suggest that stratification may have limited the vertical scale of turbulent eddies. The remainder of this section examines further evidence for inhibition of mixing by stratification. Stratification introduces an upper limit to the eddy scale, called the Ozmidov scale, estimated here as  $l_o = (P/N^3)^{1/2}$  (the usual definition is  $(\epsilon/N^3)^{1/2}$ , where  $\epsilon$  is the rate turbulent energy is dissipated by viscosity, but  $\epsilon$  and  $P$  differ only by a factor of  $1 - \Gamma$ , where the mixing efficiency  $\Gamma$  is typically 0–0.2 [Monin and Yaglom, 1975]). Ozmidov scales were calculated for every hour of positive production and stable stratification in inner and outer BBLs ( $z = 0.2$ – $0.4$  and  $0.4$ – $0.9$  m). The tenth, fiftieth, and ninetieth percentiles of the  $l_o$  probability distributions were, respectively, 0.04, 0.3, and 2.4 m for the inner BBL, and 0.05, 0.2, and 0.9 m for the outer BBL. Therefore,  $l_o$  was sometimes less than  $\kappa z$ , providing further evidence that stratification limited near-bed turbulence. Since the largest eddies contribute most to the Reynolds stress, the observed  $l_o$  suggest that ADP vertical resolution (0.015 m) was likely sufficient to resolve the much of the Reynolds stress, particularly near the bed where production was greatest.

Stratification may sometimes have inhibited turbulence so strongly that the largest turbulent scales were only moderately larger than the scales on which molecular dissipation acts directly. Molecular viscosity directly removes turbulent energy at the Kolmogorov scale  $(\nu^3/\epsilon)^{1/4}$ , while having little direct effect on eddies with much larger scales. For cases with positive  $P$ , probability distributions were calculated for  $l_k = (\nu^3/P)^{1/4}$ , which is comparable to the Kolmogorov scale. The tenth, fiftieth, and ninetieth percentiles of  $l_k$  distributions were, respectively, 3, 5, and 9 mm for the inner BBL, and also 3, 5, and 9 mm for the outer BBL. The ratio of Ozmidov to Kolmogorov scales specifies the range of turbulent eddy scales. The tenth, fiftieth, and ninetieth percentiles for this ratio were 5, 80, and 600 for the inner BBL, and 8, 50, and 300 for the outer BBL. Theories used to estimate turbulent dissipation rates from frequency spectra [Lorke and Wüest, 2005] or structure functions [Wiles et al., 2006] often assume the presence of an "inertial subrange" of scales that are much larger than  $l_k$ , yet much smaller than  $l_o$ . For a significant minority of cases observed here, small  $l_o/l_k$  ratios suggest that an inertial subrange may not have existed (for both inner and outer BBL cases,  $l_o/l_k < 10$  in 17% of cases). These small  $l_o/l_k$  ratios occurred when flows were weak and stratification was

substantial. From the definitions of  $l_o$  and  $l_k$ , it follows that  $(l_o/l_k)^{4/3} = Re_b$ , where  $Re_b = P/(vN^2)$  resembles the “buoyancy Reynolds number”  $\epsilon/(vN^2)$ , which is often used to describe stratified turbulence. The observed  $l_o/l_k$  distributions imply tenth, fiftieth, and ninetieth percentiles for  $Re_b$  were 9, 300, and 6000 for the inner BBL, and 10, 100, and 2000 for the outer BBL. Therefore, most, but not all, buoyancy Reynolds numbers exceeded 15–25.  $Re_b$  values below this range are associated with a collapse of turbulence associated with buoyancy and viscosity [Stillinger et al., 1983; Ivey and Imberger, 1991].

#### 4. Models for Turbulent Stress and Production Within the Boundary Layer

Examination of the BBL energy balance (1) begins in this section with testing of simple models for turbulent production. Observations are used to test applicability of the “Law-Of-the-Wall” (LOW), which often provides useful estimates of bottom drag, but which has sometimes been found to be inaccurate in stratified or oscillating BBLs [Freidrichs and Wright, 1997; Trowbridge et al., 1999; Lorke et al., 2002; Fugate and Chant, 2005; Perlin et al., 2005]. Consistent with inhibition of BBL turbulence by stratification (section 3), the predictions of LOW models will prove to be inaccurate. Nevertheless, after tuning, a simple parameterization for turbulent production will be shown to fit observations.

Stresses are first compared with an eddy viscosity model  $(\hat{\tau}_x, \hat{\tau}_y) = -\rho v_{LOW}(\partial u/\partial z, \partial v/\partial z)$ , where the eddy viscosity  $v_{LOW} = \kappa^2 z^2 |\partial \vec{u}/\partial z|$  is chosen to be consistent with the LOW [Monin and Yaglom, 1975]. Modeled and observed stresses tended to have the same sign, as might be anticipated from the mostly positive shear production reported in section 3, but differed in magnitude, particularly in the upper BBL (in Figure 3, compare color scales for Figures 3e and 3f with Figures 3g and 3h). Similarly, the modeled turbulent production  $v_{LOW} |\partial \vec{u}/\partial z|^2$  exceeded observed production (compare color scales in Figures 3i and 3j).

The LOW predicts a unidirectional velocity  $U$  with a logarithmic dependence on elevation:

$$U = \frac{u_*}{\kappa} \ln(z/z_0), \quad (3)$$

where the friction velocity  $u_* = (|\vec{\tau}_b|/\rho)^{1/2}$ ,  $\vec{\tau}_b$  = bed stress, and  $z_0$  is the bottom roughness length [Monin and Yaglom, 1975]. Each hour,  $U$  was calculated as the mean velocity in direction  $\vartheta$ , with  $\vartheta$  chosen to maximize  $\int_{0.15m}^{0.25m} U^2 dz$ . Then  $u_*$  was estimated by fitting (3) to profiles of  $U$  measured 0.15–0.25 m above the bed. A single roughness  $z_0 = 6 \times 10^{-4}$  m, chosen to optimize the fit of (3) to observed mean flow profiles, was applied to all observations.

In the elevation range  $z = 0.15$ – $0.25$  m, good agreement was found between fitted and observed velocity profiles (Figure 4). Fair agreement is to be expected, because  $u_*$  and  $z_0$  were chosen to optimize fit at these elevations. At higher elevations, observations depart from (3), possibly owing to stratification and time dependence of the flow [Lorke et al., 2002; Brink and Lentz, 2010].

The LOW bed stress estimate  $\vec{\tau}_{LOW}$  is defined to have direction  $\vartheta$  and magnitude  $\rho u_*^2$ , with  $u_*$  determined by fitting (3). A more direct bed stress estimate was  $\vec{\tau}_b = \vec{\tau}_{15} + \vec{\tau}(t)$ , where  $\vec{\tau}_{15}$  was the Reynolds stress estimated from the ADP at the lowest reliable measurement elevation  $z = 0.15$  m, and the estimated stress variation between 0.15 m and the bed,  $\vec{\tau}(t)$ , was calculated from the boundary layer momentum equation (Appendix B) but was small (by regression,  $\tau_{b,x} + i\tau_{b,y} = 1.08e^{i\psi\pi/180}(\tau_{15,x} + i\tau_{15,y})$ , with  $r^2 = 0.88$  and  $\psi = 7^\circ$ ). The LOW stress estimate was strongly correlated with, but about 4 times larger than, the more direct bed stress estimate (Figure 5a. By regression,  $\tau_{b,x} + i\tau_{b,y} = 0.27e^{i\psi\pi/180}(\tau_{LOW,x} + i\tau_{LOW,y})$ , with  $r^2 = 0.79$  and  $\psi = 4^\circ$ ). This tendency for fitting of logarithmic velocity profiles to overestimate stress could not be explained by unstratified viscous sublayer effects: the elevation in wall units  $zu_*/\nu$  usually exceeded 100, well above the minimum value of 30 required for application of the log law [Spalding, 1961]. The failure of the LOW within 0.25 m of the bed is notable, because the accuracy of the LOW is expected to improve as the bed is approached [Lorke et al., 2002].

Next, we test the LOW prediction

$$\tau_{pred,y} = -\rho C_D |v_1| v_1, \quad (4)$$

where the drag coefficient  $C_D$  equals  $[\kappa/\log(1\text{ m}/z_0)]^2$ , and  $v_1$  = along-lake velocity 1 m above the bed. Since the across-lake velocity at  $z = 1$  m (denoted  $u_1$ ) was small, the term  $|v_1|$  in (4) was chosen instead of the more



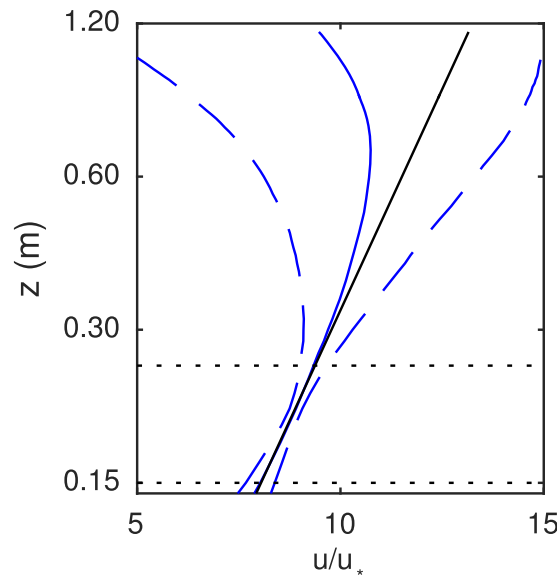


**Figure 4.** Vertical profiles of velocity in the dominant flow direction  $u$  normalized by fitted friction velocity  $u_*$ . Solid blue line indicates mean over all 696 hourly profiles, dashed blue line indicates  $\pm 1$  standard deviation, solid black line indicates fitted logarithmic profile, and dotted black lines indicate range of elevations used for fitting.

conventional term  $(u_1^2 + v_1^2)^{1/2}$  to simplify subsequent modeling of wave propagation. The LOW again overpredicted observed bed stress (Figure 5b). However, after abandoning the LOW drag coefficient, and instead choosing a coefficient  $C_D = 1.54 \times 10^{-3}$  to optimally fit the dominant along-lake stress, (4) was in fair agreement with observations; by linear regression,  $\tau_{b,y} = 1.0\tau_{\text{pred},y} - 3.8 \times 10^{-5}$  Pa with  $r^2 = 0.64$ . Although  $C_D$  is purely empirical and differs from the LOW prediction, drag coefficients in the range  $1-3 \times 10^{-3}$  are common in lakes and oceans [Wüest and Lorke, 2003; Simpson et al., 2014; Munk and Wunsch, 1998].

When averaged over a wave period, the vertically integrated boundary layer turbulent production equals  $\tau_{b,x}u_1 + \tau_{b,y}v_1$  [Sleath, 1984, section 5]. To simplify subsequent modeling, the contribution  $\tau_{b,x}u_1$  is assumed negligible, based on the small measured values of  $u_1$  and  $\tau_{b,x}$  (the accuracy of this approximation is assessed in section 6). Therefore, wave-averaged boundary layer turbulent production was estimated from daily-mean  $\tau_{\text{pred},y}v_1$ , which ranged between  $4 \times 10^{-6}$  and  $4 \times 10^{-5}$  W m $^{-2}$  (black curve, Figure 6a).

## 5. A Model for Wave Propagation Above the Boundary Layer

Having examined turbulent production (the right of (1)) in section 4, we next consider the vertical wave propagation that is associated with the supply of wave energy to the boundary layer (the left of (1)). In this section, the structure of above-BBL flows is used to quantify internal wave propagation and reflection.

The power spectrum of along-lake velocity reveals complex vertical variability across the dominant range of seiche frequencies (0.9–2.35 cycles/d; Figure 7a). Within 1 m of the bed, flows were attenuated by BBL

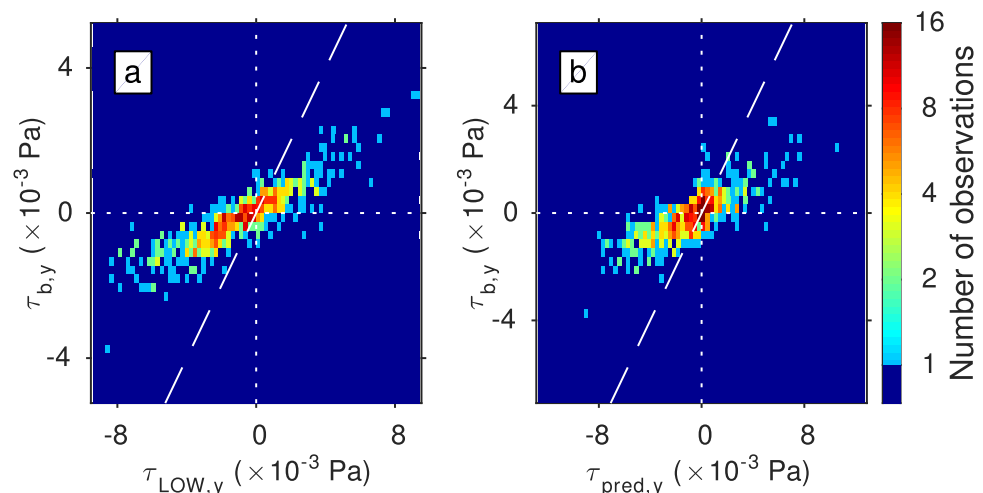


**Figure 5.** Comparison between all 696 hourly-mean along-lake bed stress values estimated from turbulence measurements ( $\tau_{b,y}$ ) and corresponding values inferred from the LOW. (a) LOW stress estimates  $\tau_{\text{LOW},y}$  made by fitting logarithmic profiles to hourly-mean velocities measured 0.15–0.25 m above the bed. (b) LOW stress estimates  $\tau_{\text{pred},y}$  made using fitted bottom roughness  $z_0$  and hourly-mean velocities measured 1 m above the bed. Colors indicate the number of hours falling within each pixel. White dashed line indicates agreement between observations and LOW theory.

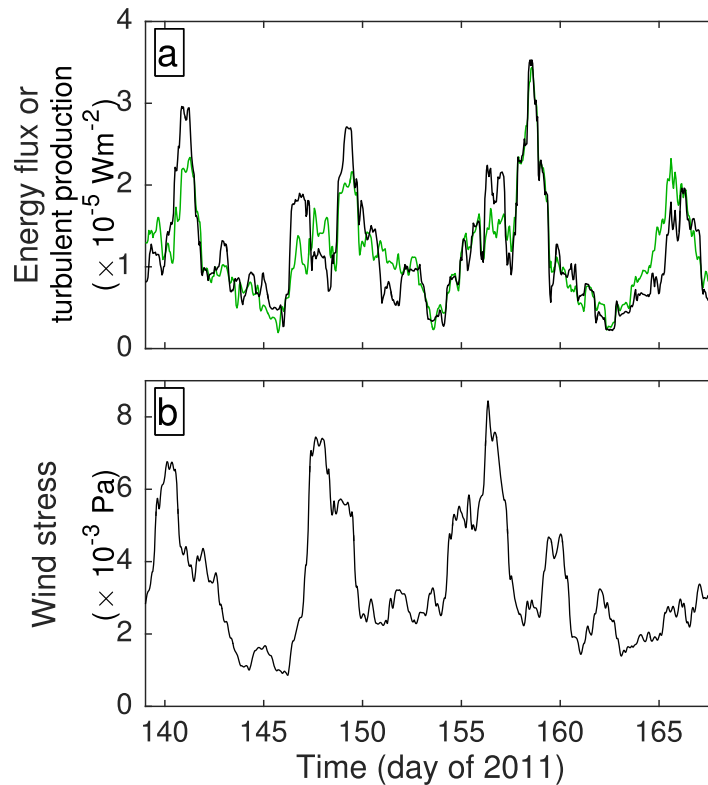


**Figure 6.** Daily running mean time series of (a) BBL turbulent production (black) and net wave energy flux to the lakebed (green); (b) magnitude of 1–3 cycle/d fluctuations in along-lake wind stress.

turbulent friction. At higher elevations, it is hypothesized that much of the vertical variability arises from interference between incident and partially reflected internal waves.

If internal wave reflection is responsible for the above-BBL velocity structure, then fitting of internal wave theory to the observed velocity structure can provide an estimate the reflection coefficient  $R = (\text{reflected wave amplitude})/(\text{incident wave amplitude})$ . If the observed spectral minimum labeled 1 in Figure 7a were associated with a node, then destructive interference would reduce velocity amplitudes there by the factor  $1 - R$ . Similarly, if the spectral maximum labeled 2 were associated with an antinode, then constructive interference would increase velocity there by  $1 + R$ . Now the ratio between velocity variances at points 1 and 2 equals  $(1 - R)^2 / (1 + R)^2$ . The observed power spectral ratio 0.4

then suggests the reflection coefficient  $R = 0.23$ . Such a low reflection coefficient is inconsistent with classical seiche theory (which assumes  $R = 1$ ), but is consistent with the observations that seiche energy in this lake propagates vertically.

To obtain more systematic estimate of  $R$ , consider a theoretical velocity associated with internal waves  $v_w$ , which will be fitted to the measured velocity  $v$ . Both velocities are represented by Fourier series

$$v_w(z, t) = \sum_{\sigma} \langle v_w(z) \rangle_{\sigma} e^{i2\pi\sigma t}, \quad v(z, t) = \sum_{\sigma} \langle v(z) \rangle_{\sigma} e^{i2\pi\sigma t}, \quad (5)$$

where, for any variable  $X$ ,  $\langle X \rangle_{\sigma}$  denotes the frequency- $\sigma$  complex amplitude of  $X$ . The theoretical velocity is the sum of incident and reflected components

$$\langle v_w(z) \rangle_{\sigma} = (N/N_0)^{1/2} \langle v_d \rangle_{\sigma} \left[ e^{-i\phi_w(z)} + R e^{i\phi_w(z)} \right], \quad (6)$$

where  $\langle v_d \rangle_{\sigma}$  is the complex amplitude of downward-propagating waves at the bed, the factor  $(N/N_0)^{1/2}$  accounts for WKB focusing [Leaman and Sanford, 1975],  $N_0$  is the value of  $N$  at the bed, and the theoretical phase between  $\langle v_d \rangle_{\sigma}$  and velocity at elevation  $z$  is

$$\phi_w(z) = \int_{z'=0}^z \frac{2\pi}{\lambda_z} dz' = \int_{z'=0}^z \frac{N}{\sigma \lambda_y} dz'. \quad (7)$$

Here  $\lambda_z$  and  $\lambda_y$  are vertical and horizontal wavelengths, and the second equality of (7) follows from the internal wave dispersion relation for  $\sigma \ll N$  [Henderson and Deemer, 2012]. The above theory for  $v_w$  accounts for the effects of within-BBL energy loss on waves above the BBL by inclusion of a reflection coefficient, which may take values less than 1. However, the theory does not explicitly include BBL friction, and does not apply within the BBL. The velocity “at the bed”  $\langle v_d \rangle_{\sigma}$  is simply a convenient reference, taken as the velocity that would be observed given nondissipative propagation all the way to the bed. Along-lake bed slope and

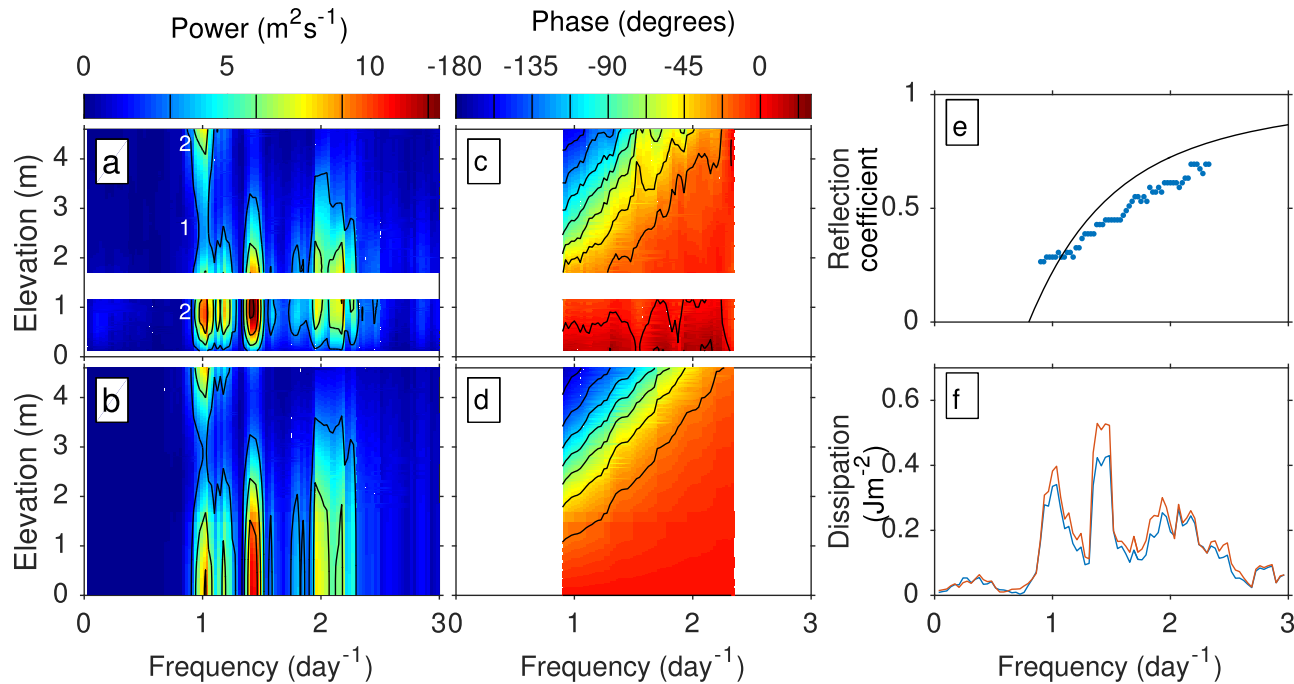


**Figure 7.** Frequency dependence of (a, b) velocity variance, (c, d) phase, (e) reflection coefficient, and (f) boundary layer dissipation. Power spectra of (a) measured along-lake velocity  $v$  and (b) fitted velocity  $v_w$ . (c) Measured phase  $\phi$  and (d) fitted phase  $\phi_w$  of along-lake velocity, with negative phase indicating a lag behind fitted near-bed velocity. (e) Reflection coefficient estimated from wave propagation model ( $R$ , blue dots) and predicted by drag coefficient model ( $R_{pred}$ , black curve). (f) Spectral density of vertically integrated boundary layer dissipation calculated from measured Reynolds stress ( $D(\sigma)$ , blue) and linearized drag coefficient model ( $D_{lin}(\sigma)$ , red).

wave nonlinearity have been neglected. The vertical structure of  $N$  was estimated by fitting a smooth curve through the deployment-averaged density profile, with density calculated from measured temperature.

For each frequency  $\sigma$ , a reflection coefficient  $R(\sigma)$  was chosen to minimize the model error  $\mathcal{E}$  above the wave boundary layer ( $1 \text{ m} < z < 4.5 \text{ m}$ ) within a band of frequencies centered on  $\sigma$ :

$$\mathcal{E}(\sigma) = \int_{\sigma' = \sigma - \Delta\sigma}^{\sigma + \Delta\sigma} \int_{z=1 \text{ m}}^{4.5 \text{ m}} |\langle v(z) \rangle_{\sigma'} - \langle v_w(z) \rangle_{\sigma'}|^2 dz d\sigma', \quad (8)$$

where the bandwidth  $\Delta\sigma = 0.08 \text{ day}^{-1}$  was required for statistical stability (a single complex amplitude  $\langle v_d \rangle_{\sigma}$  was also chosen for each frequency). Possibly owing to lake geometry, a narrow range of horizontal wavelengths  $\lambda_y$  minimized  $\mathcal{E}(\sigma)$  (for all  $\sigma$  between  $0.9$  and  $2.35 \text{ day}^{-1}$ ,  $1085 \text{ m} < \text{optimal } \lambda_y < 1365 \text{ m}$ , which is about twice the lake length at the depth of ADP measurements, consistent with a horizontally standing seiche). A single horizontal wavelength  $\lambda_y = 1290 \text{ m}$ , which minimized the total error  $\int_0^{6 \text{ day}^{-1}} \mathcal{E}(\sigma) d\sigma$ , was chosen (from this wavelength, the internal Rossby radius was estimated as  $(\text{wave speed})/f = (1290 \text{ m}/17 \text{ h})/(10^{-4} \text{ s}^{-1}) = 210 \text{ m}$ ). Agreement between fitted and observed power spectra above the bottom boundary layer (Figures 7a and 7b) indicates consistency with the hypothesis that minima and maxima in depth-dependent spectra are nodes and antinodes of partially reflected internal waves. At the top of the boundary layer ( $z = 1 \text{ m}$ ), observed spectra slightly exceeded fitted spectra. As expected, within the boundary layer ( $z < 1 \text{ m}$ ), turbulent friction reduced observed spectra below the fitted (frictionless) spectra.

The observed phase  $\phi(z)$  is defined as the argument of  $\langle v(z) \rangle_{\sigma} \langle v_d \rangle_{\sigma}^*$ , where  $*$  denotes a complex conjugate. Observed and fitted phases matched outside the boundary layer (Figure 7c,d). An almost linear dependence of phase on elevation is clear at low frequencies, consistent with net upward phase propagation, implying downward energy propagation. The tendency for  $|\partial\phi/\partial z|$  to decline with increasing frequency indicates a vertical wavelength  $\lambda_z$  increasing with frequency, consistent with the fitted constant horizontal wavelength  $\lambda_y$  (7). Observed phases were positive near the bed (Figure 7c, energy-weighted near-bed mean phase =  $16^\circ$ ), indicating a near-bed phase lead, as is typical of oscillating turbulent boundary layers [Sleath, 1984; Lorke et al., 2002]. Phases are plotted only for the energetic frequencies  $0.9 \text{ day}^{-1} < \sigma < 2.35 \text{ day}^{-1}$ .

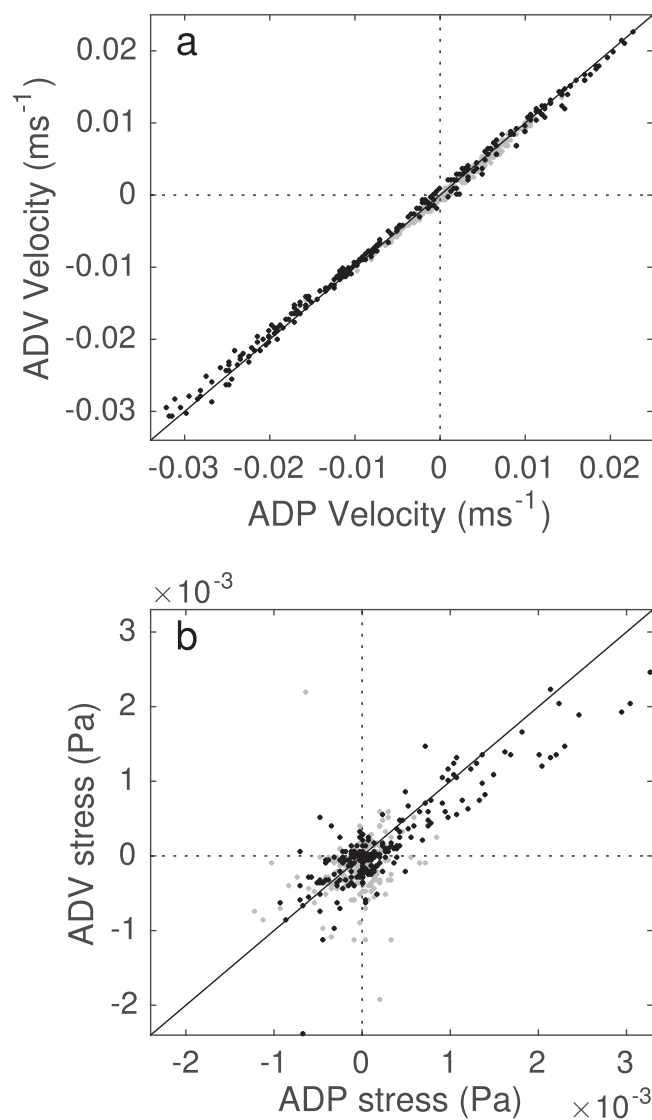


**Figure 8.** Comparison between ADV and ADP estimates of (a) hourly-mean velocity and (b) Reynolds stress. Black and grey dots, respectively, along-lake and across-lake components.

about 250%. Furthermore, above the outer-BBL variance maximum, the Stokes model predicts phase variations for total (as opposed to defect) velocity of  $<5^\circ$ , whereas observed phase variations ranged up to  $180^\circ$ . An alternative BBL model, which also neglects wave propagation but assumes an eddy viscosity linearly proportional to elevation [Mei, 1989, section 8.7.1], yields predictions similarly at odds with observations.

## 6. Energy Balance

Turbulent production will now be compared with internal wave absorption and reflection. First, to facilitate comparison with frequency-dependent wave reflection, the frequency dependence of BBL turbulent production will be examined. Equating production with the energy supplied by internal waves will then yield a model predicting the frequency-dependent reflection coefficient. This section will conclude with a comparison between time series of turbulent production and energy supply.

Since vertically integrated BBL turbulent production is roughly  $\tau_{b,y}v_1$  (section 4), the spectral density of production, representing energy loss for waves with frequency  $\sigma$ , is

At frequencies above  $2.35 \text{ day}^{-1}$ , vertical wavelengths became so large that  $v_w$  was almost depth uniform for  $1 \text{ m} < z < 4.5 \text{ m}$ , and fits were poorly constrained with fitted  $R$  fluctuating wildly (not shown). At frequencies below  $0.9 \text{ day}^{-1}$ , (6) provided a poor fit to observations.

The fitted reflection coefficient  $R$  increased with frequency (blue dots, Figure 7e), ranging from 0.3 at  $\sigma = 0.9 \text{ day}^{-1}$  to 0.7 at  $\sigma = 2.35 \text{ day}^{-1}$ . This is a leading-order departure from the perfect reflection ( $R = 1$ ) assumed by classical internal seiche theories. Since energy reflection is proportional to  $R^2$ , these reflection coefficients suggest that only a minority of incident energy was reflected, with most lost to turbulent production in the BBL.

The above analysis has shown that the vertical and frequency-domain variability of above-BBL velocities was consistent with a model for partially reflected, vertically propagating internal waves. In contrast, above-BBL velocities were inconsistent with oscillating BBL models that neglect vertical wave propagation, such as the Stokes boundary layer model [Lorke *et al.*, 2002]. For the Stokes model, which assumes a constant eddy viscosity, outer-BBL velocity variance is enhanced  $<15\%$  relative to overlying velocity, whereas the observed enhancement between points 1 and 2 of Figure 7a was



$$D(\sigma) = \Re\{\Phi_\sigma(\tau_{b,y}, v_1)\}, \quad (9)$$

where  $\Re$  denotes the real part and  $\Phi_\sigma(X, Y)$  is the cross-spectral density between  $X$  and  $Y$ . Wave energy loss  $D(\sigma)$  was most intense at frequencies  $0.9\text{--}2.4 \text{ day}^{-1}$  (blue curve, Figure 7f). It would be natural to model this energy loss as  $\Re\{\Phi_\sigma(\tau_{\text{pred},y}, v_1)\}$ , but the absolute value in (4) (i.e., the term  $|v_1|$ ) would make subsequent analysis intractable. Instead, we use the expression

$$D_{\text{lin}}(\sigma) = (8/\pi)^{1/2} \rho C'_D v_{\text{rms}} \Phi_\sigma(v_1, v_1), \quad (10)$$

where  $v_{\text{rms}}$  and  $\Phi_\sigma(v_1, v_1)$  are the root-mean-square and the power spectral density of  $v_1$ . This approximation is obtained by substituting (4) into (9) and replacing  $|v_1|$  with  $(8/\pi)^{1/2} v_{\text{rms}}$ , where the factor  $(8/\pi)^{1/2}$  is chosen to ensure correct prediction of total wave energy loss when  $v_1$  has a Gaussian distribution (i.e., to ensure  $\int D_{\text{lin}}(\sigma) d\sigma = \int D(\sigma) d\sigma$ ). Agreement was found between the full expression (9) and the approximation (10), with best fit  $C'_D = 1.56 \times 10^{-3}$  (compare blue and red lines, Figure 7f). The similarity of  $C'_D = 1.56 \times 10^{-3}$  and  $C_D = 1.54 \times 10^{-3}$  (section 4) indicates success of the linearized, Gaussian approximation.

For simplicity, we have neglected  $\tau_{b,x}u_1$ . This approximation was motivated by the observed dominance of along-lake velocity and stress (section 3), and direct calculations confirm that the neglected contribution was small (when both contributions were retained,  $\tau_{b,x}u_1$  contributed 17% to the integrated wave energy loss  $\int_{0.09 \text{ day}^{-1}}^{2.35 \text{ day}^{-1}} D(\sigma) d\sigma$ , not shown).

To derive a prediction for the reflection coefficient, nonlinear energy transfers between frequencies [Horn et al., 2001; de la Fuente et al., 2010] are neglected, so that the energy balance (1) can be applied at every frequency. Now, at each frequency, boundary layer wave energy loss  $D(\sigma)$  balances the net energy flux  $F_I(\sigma) - F_R(\sigma)$  supplied by propagating waves. Incident waves with frequency  $\sigma$  transport energy to the boundary layer at a rate  $F_I(\sigma) = E_d(\sigma)c_g(\sigma)$ , where  $E_d$  is the incident wave energy and the vertical component of the group velocity

$$c_g(\sigma) = 2\pi\lambda_y\sigma^2/N. \quad (11)$$

Reflected waves have energy  $R^2E_d(\sigma)$ , and transport energy away from the BBL at a rate  $F_R(\sigma) = R^2E_d(\sigma)c_g(\sigma)$ . Therefore, the net supply of wave energy to the BBL is

$$F_I(\sigma) - F_R(\sigma) = (1 - R^2)E_d(\sigma)c_g(\sigma). \quad (12)$$

To relate the total wave energy to  $v_1$ , note that the bed is a node of potential energy (so total energy = kinetic energy at the bed), and from (6) the total velocity at the bed is  $(1 + R)v_d$ , so

$$E_d(\sigma) = \frac{\rho \Phi_\sigma(v_1, v_1)}{2(1 + R)^2}. \quad (13)$$

Requiring  $F_I(\sigma) - F_R(\sigma) = D_{\text{lin}}(\sigma)$  and combining (10), (11), (12), and (13) yields a predicted reflection coefficient

$$R_{\text{pred}}(\sigma) = \frac{1 - \alpha}{1 + \alpha}, \quad (14)$$

where

$$\alpha = 2 \left( \frac{8}{\pi} \right)^{1/2} C'_D \frac{v_{\text{rms}}}{c_g} = \left( \frac{8}{\pi} \right)^{1/2} \frac{C'_D N v_{\text{rms}}}{\pi \lambda_y \sigma^2} \quad (15)$$

is the predicted ratio between the wave energy loss to turbulent production and the energy supplied by downward-propagating waves. Previously, in the context of near-inertial wave reflection from the deep ocean bed, D'Asaro [1982] derived (14), with a different prediction for  $\alpha$ , using a slab model for the boundary layer. Henderson and Deemer [2012] suggested that the parameter  $\alpha$  may control the propagation and reflection of internal seiches.

The prediction of (14)–(15) is roughly consistent with reflection coefficients calculated in section 5 (compare black line with blue dots, Figure 7e). Two free parameters were required to estimate reflection coefficients:

$\lambda_y$  and  $C'_D$ . Using velocities measured above the BBL,  $\lambda_y$  was chosen to minimize  $\mathcal{E}$  in (8). Using  $v_1$  and turbulent stresses measured within the BBL,  $C'_D$  was chosen to fit  $D_{lin}(\sigma)$  to  $D(\sigma)$ . Therefore,  $C'_D$  was determined from different data than  $\lambda_y$ , and no parameters were tuned to ensure the agreement between predicted and observed reflection coefficients.

To estimate a time-dependent net wave energy flux, let  $\mathcal{F}^{1/2}(t)$  be the time series whose Fourier transform is

$$\langle \mathcal{F}^{1/2} \rangle_\sigma = \frac{\sqrt{[1 - R_{pred}^2(\sigma)] \rho C_g(\sigma)}}{1 + R_{pred}(\sigma)} \langle v_1 \rangle_\sigma. \quad (16)$$

Now, given time-independent reflection coefficients, the wave-averaged value of  $\mathcal{F}(t) = [\mathcal{F}^{1/2}(t)]^2$  is the net supply of wave energy to the boundary layer (i.e.,  $F_I - F_R$ ). Daily averaged  $\mathcal{F}$  balanced the boundary layer turbulent production  $\tau_y v_1$  (compare black and green curves of Figure 6a).

Since the observed waves were likely generated by oscillating winds, the bursts of energy flux evident in Figure 6a might result from passing weather systems. Using winds measured at Troutdale Airport, 4 km distant, the along-lake wind stress was estimated as  $\tau_w = \rho_a C_{Da} |\vec{v}_w| v_w$ , where  $\rho_a = 1.3 \text{ kg m}^{-3}$  is the air density,  $C_{Da} = 1.3 \times 10^{-3}$  is the air-side drag coefficient,  $|\vec{v}_w|$  = wind speed, and  $v_w$  = along-lake wind velocity. To isolate the fluctuations responsible for generating internal waves, a filtered time series  $\tau'_w$  was calculated by band-passing  $\tau_w$  between 1 and 3 cycles/d. Three peaks in daily averaged  $|\tau'_w|$  were observed (Figure 3f). All were followed, after 0.8–2.2 days, by peaks in wave energy flux and boundary layer turbulent production (Figure 3e). The lag is comparable to the time taken for internal waves to propagate to the lakebed [Henderson and Deemer, 2012]. A fourth peak in lakebed production, on day 166, was unexplained by any burst in measured wind stress (Figure 6). The reason for this fourth peak in wave energy flux is unclear. It is possible that fluctuating winds over Lacamas Lake generated this fourth peak, but were not measured at Troutdale Airport owing to spatial variability of the wind field.

## 7. Discussion and Conclusions

Despite the complex boundary layer dynamics observed in Lacamas Lake, a simple model successfully predicted wave absorption and reflection. One complex feature of BBL dynamics was a fluctuation in stratification through the wave cycle, possibly owing to SIPs. Even within just 0.4 m of the bed, high Richardson numbers (ranging from  $<0.07$  to  $>0.7$ ) and low Ozmidov scales (sometimes less than elevation above the bed) suggested periodic inhibition of mixing by stratification.

Despite the complications outlined above, and nonlinearity of the bottom drag law, a linearized model (10) successfully predicted observed frequency-dependent loss of wave energy to turbulence. Consistent with theoretical expectations for the small-amplitude seiche [Horn *et al.*, 2001], the neglect of within-BBL nonlinear transfers of seiche energy to smaller-scale waves did not lead to major errors in the energy balance. The estimated drag coefficient was  $1.56 \times 10^{-3}$ , less than a value sometimes used to estimate oceanic dissipation ( $2.5 \times 10^{-3}$ ) [Munk and Wunsch, 1998], although this difference may be insignificant given the range of reported coefficients. Despite neglect of further potential complications associated with bed slope, a simple linearized energy balance approximately predicted observed frequency-dependent reflection coefficients. Despite neglect of temporal variations in reflection coefficients, estimates of net wave energy flux to the boundary layer matched observed turbulent production.

A simple model ((14) and (15)) predicts that reflection is controlled primarily by the ratio between near-bed water flow speed and vertical wave propagation speed. Waves in Lacamas Lake had very small propagation speeds ( $\sim 1 \times 10^{-4} \text{ m s}^{-1}$  at 1 cycle/d), ensuring that the boundary layer could absorb the slowly supplied energy with minimal reflection. At higher frequencies, wave speeds (11) and reflection coefficients increased.

The importance of wave speed is highlighted by the contrast between absorption of waves in Lacamas Lake and strong reflection of near-inertial waves in the abyssal ocean [D'Asaro, 1982]. Both types of waves have similar frequency and encounter similar boundary layer turbulent production [St. Laurent and Garrett, 2002], but waves in Lacamas have smaller vertical wavelengths ( $\sim 10 \text{ m}$ , compared with  $>100 \text{ m}$  in the ocean) and therefore smaller vertical propagation speeds. The small vertical wavelengths can in turn be traced to small lateral wavelengths, which are to be expected in small lakes. Therefore, weak reflection is

favorable in small lakes (strong near-bed stratification has potential to reinforce this trend, (11)). This analysis largely confirms *Henderson and Deemer's* [2012] speculation regarding factors conducive to vertical propagation. To make these ideas more concrete, consider four cases: a very small lake with strong near-bed stratification (lake length 400 m,  $N = 2 \times 10^{-2} \text{ s}^{-1}$ ), a very small lake with weak stratification (length 400 m,  $N = 4 \times 10^{-3} \text{ s}^{-1}$ ), a moderate length (narrow) lake with strong stratification (length 2 km,  $N = 2 \times 10^{-2} \text{ s}^{-1}$ ), and moderate length lake with weak stratification (length 2 km,  $N = 4 \times 10^{-3} \text{ s}^{-1}$ ). Taking  $C_D = 10^{-3}$ ,  $\lambda_y =$  twice lake length,  $v_{rms} = 0.01 \text{ m s}^{-1}$ , and substituting into (14) and (15) gives reflection coefficients for the respective cases of 0.02, 0.68, 0.68, and 0.93.

Although vertical propagation is clear in measurements obtained from several other small lakes [*Serra et al.*, 2007, Figure 8; *LaZerte*, 1980, Figures 6 and 8; *Vidal et al.*, 2008, Figures 5 and 8], several factors may limit the applicability of the model tested here to other lakes. The narrowness of Lacamas Lake and low along-lake bed slope made a one-dimensional, horizontal-bed model a good approximation. Generalization to two dimensions is possible [*D'Asaro*, 1982], although substantial across-lake variability of the flow field is expected if the internal Rossby Radius is substantially smaller than the lake's smallest dimension. The horizontal-bed approximation may be more difficult to relax, and reflection is likely to become more complex as the bed slope approaches the slope of wave characteristics, along which wave energy propagates [*Slinn and Riley*, 1996].

## Appendix A: Reynolds Stress Estimation

### A1. Overview

Reynolds stress profiles are routinely calculated using measurements from four-beam ADP systems [*Lu and Lueck*, 1999]. An intermediate step in this calculation requires the grouping of the four beams into two pairs, and within-pair differencing of along-beam velocity variances. For this approach, the two beams of a pair must be tilted by equal angles in opposite directions from the vertical. This requirement cannot be met using a single three-beam ADP. However, the requirement can be met by pairing beams from different instruments when two three-beam ADPs are arranged as ADPs 1 and 2 are in Figure 2. The three resulting beam-pairs yield an overspecified problem for the two components of Reynolds stress (i.e.,  $\overline{u'w'}$  and  $\overline{v'w'}$ ), which was solved here by least squares. This method resembles the more general approach of *Vermeulen et al.* [2011] although, unlike *Vermeulen et al.*, no attempt was made here to synchronize ADPs to prevent simultaneous measurements.

### A2. Detailed Method

Let  $V_{i,j,k}(t)$  be the velocity measured by instrument  $i$  ( $i = 1$  or  $2$  for the two downward-looking instruments), acoustic beam  $j$  ( $j = 1, 2$ , or  $3$ , positive  $V$  for velocity away from instrument, numbered so that beam  $j$  of instrument 1 and beam  $j$  of instrument 2 are tilted by equal angles in opposite directions from vertical), and elevation bin  $k$  at time  $t$ . Following the approach used when evaluating mean flows (section 2), low ( $<90\%$ ) correlation cases were removed. Fixing attention on a single instrument, beam, and rangebin (i.e., fixed  $i, j$ , and  $k$ ), and on a single hour of the deployment (e.g., between 1 and 2 A.M. on 1 June) yields a single 1 h velocity time series. A quadratic function of time was fitted to this 1 h time series. The turbulent velocity time series  $V'_{i,j,k}(t)$  was defined as the departure of 1 h velocity time series from the fitted quadratic. This process was repeated to calculate turbulent velocities for every hour, rangebin, beam, and instrument. Although conventional, this approach for separating turbulence from wave motions may face difficulties if waves contribute substantial velocity variance on time scales of less than an hour. Fortunately, the velocity variance of internal waves is dominated by time scales comparable to a day (section 5). Observations of atmospheric [*Kaimal et al.*, 1972] and estuarine [*Trowbridge et al.*, 1999] boundary layers suggest that much of the Reynolds stress is carried by eddies with periods of order elevation/(mean velocity), which for these observations gives periods comparable to a minute.

Let  $\vec{b}_j$  be a horizontal unit vector pointing from beam  $j$  of instrument 2 to beam  $j$  of instrument 1, and let  $\mu_j$  be the water velocity in direction  $\vec{b}_j$ . Now, following the approach used for four-beam ADPs, for a given hour at the  $k$ 'th elevation bin, the Reynolds stress is estimated from beam pairs as

$$\overline{\mu_j' w'} = \frac{\text{var}[V'_{1,j,k}] - \text{var}[V'_{2,j,k}]}{2\sin(2\varphi)} \quad (\text{A1})$$

where  $\varphi = 25^\circ$  is the beam angle from vertical, and  $\text{var}$  indicates a variance evaluated for the hour-long time series [Lohrmann *et al.*, 1990]. Conversion from the three directions ( $\vec{b}_1, \vec{b}_2, \vec{b}_3$ ) associated with the beam pairs to the two ( $u, v$ ) directions is then achieved by finding the  $X_k$  that yields the least squares solution to the overspecified matrix problem  $\sum_k A_{j,k} X_k = B_j$ , where

$$A = - \begin{bmatrix} \cos(h), & \sin(h) \\ \cos(h+120^\circ), & \sin(h+120^\circ) \\ \cos(h-120^\circ), & \sin(h-120^\circ) \end{bmatrix}, \quad (\text{A2})$$

$$X = \begin{bmatrix} \overline{u'w'} \\ \overline{v'w'} \end{bmatrix}, \quad (\text{A3})$$

$$B = \begin{bmatrix} \overline{\mu'_1 w'} \\ \overline{\mu'_2 w'} \\ \overline{\mu'_3 w'} \end{bmatrix}, \quad (\text{A4})$$

and  $h$  = angle counterclockwise from direction of  $u$  to direction of  $\vec{b}_1$  (the corresponding angles to  $\vec{b}_2$  and  $\vec{b}_3$  are  $h+120^\circ$  and  $h-120^\circ$ ).

### A3. Comparison With Alternative Reynolds Stress Estimates

To test the accuracy of this method for Reynolds stress estimation, a tripod was deployed from 15 to 24 July 2011, mounted with an ADV sampling at  $z = 0.31$  m, and two downward-looking ADPs sampling every 0.015 m from  $z = 0.15$  m to  $z = 1.14$  m. The ADV sampled continuously at 4 Hz. ADP 1 recorded with 0.5 s single-sample duration, 550 s burst duration, and 600 s repeat interval, whereas ADP 2 recorded with 0.5 s single-sample duration, 2 s burst duration, and 15 s repeat interval. The ADV velocity was rotated to minimize variance of the hourly-mean bed-normal velocity  $w$ . Hourly-mean bed-parallel velocities were compared, and an orientation discrepancy of  $5.5^\circ$  was found between ADP and ADV velocities, possibly resulting from a compass calibration error. This discrepancy was removed by rotating ADV velocities about the  $w$  axis, and excellent agreement with ADP hourly-mean velocities was obtained (Figure 8a). ADV-based hourly Reynolds stresses were then calculated directly from the covariance between  $w'$  and  $u', v'$ . These ADV stresses were in fair agreement with ADP-based Reynolds stress estimates at  $z = 0.315$  (Figure 8b; the dominant EOF between the two complex stresses  $\overline{u'w'} + i\overline{v'w'}$  explained 89% of the stress variance summed over the two estimates, with a best fit rotation error of  $10^\circ$  between instruments, and ADP stress magnitude  $\approx 0.91 \times$  ADV stress magnitude). Subsampling ADPs to mimic the sampling scheme used during the 19 May to 17 June deployment yielded similar results: retaining only one 0.5 s measurement from ADP 2 every 15 s (and discarding the other three measurements every 15 s), while retaining two 150 s bursts from ADP 1 every 600 s, yielded a dominant EOF between ADV and ADP stresses that explained 89% of variance, with a best fit rotation error of  $9^\circ$ , and ADV stress magnitude  $\approx 0.94 \times$  ADP stress magnitude (not shown).

Acoustic pulses emitted by one ADP have potential to interfere with the measurements made by the other ADP. The test presented here (Figure 8) establishes that such interference did not cause clear problems in this case. However, further testing would be required to establish the method's validity for other instrument arrangements and sampling schemes.

### A4. Burst Sampling

ADV and ADP Reynolds stress estimates were in agreement (section A3), despite differences between the burst sampling schemes used by the various instruments (i.e., despite differences in ADP burst duration and repeat interval). This insensitivity to burst sampling is expected, because the Reynolds stress depends on only the estimated hourly velocity variance (equation (A1)), and because subsampled time series are expected to have nearly the same variance as continuously sampled time series (so long as the time series is stationary, the single-sample duration is short, and sufficient turbulent eddies are sampled to yield stable estimates). This remains true even if burst intervals, repeat intervals, and data gaps become comparable to the time scales of stress-bearing eddies, although the scatter of estimates is slightly increased in this case [Lenschow *et al.*, 1994]. Although subsampling can preclude accurate partitioning of variance between



frequencies (i.e., power spectral estimation), Reynolds stress estimates depend on only the total variance, not on such partitioning. The relative insensitivity of estimated variance to data gaps is a special case of the insensitivity of covariance to data gaps, which boundary layer meteorologists have exploited for “disjunct eddy covariance” flux estimation [Rinne *et al.*, 2000]. Here brief bursts were used to prolong the sampling life for ADP 2, which was limited by the instrument’s 368 MB internal memory (cf. ADP 1, which was equipped with a 4 GB memory expansion). The ability of disjunct sampling schemes to reduce memory and power usage might prove useful for other applications (e.g., Turbulent dissipation can also be estimated from variances, in the form of structure functions [Wiles *et al.*, 2006]).

## Appendix B: Estimation of Stress Variation Within 0.15 m of the Bed

The leading order boundary layer momentum equations are

$$\frac{\partial(u-u_{\infty})}{\partial t} - fv + \frac{\partial\tau_x}{\partial z} = 0, \quad (B1)$$

$$\frac{\partial(v-v_{\infty})}{\partial t} + fu + \frac{\partial\tau_y}{\partial z} = 0, \quad (B2)$$

where  $(u_{\infty}, v_{\infty})$  is the velocity just above the boundary layer, here evaluated as the velocity measured at  $z = 1$  m. Integrating (B1) and (B2) from  $z = 0$  to 0.15 m yields

$$\tau_{b,x} - \tau_x|_{z=0.15\text{ m}} = \int_0^{0.15\text{ m}} \left[ \frac{\partial(u-u_{\infty})}{\partial t} - fv \right] dz, \quad (B3)$$

$$\tau_{b,y} - \tau_y|_{z=0.15\text{ m}} = \int_0^{0.15\text{ m}} \left[ \frac{\partial(v-v_{\infty})}{\partial t} + fu \right] dz. \quad (B4)$$

The correction  $\bar{\Delta}\tau = \bar{\tau}_b - \bar{\tau}_{15}$  was calculated from (B3) and (B4) by assuming that  $(u, v)$  varied linearly with  $z$ , from zero at the bed to the measured value at  $z = 0.15$  m.

## Acknowledgments

John Harrison and Bridget Deemer contributed to planning and execution of fieldwork and provided valuable comments on this manuscript. Further fieldwork assistance was provided by Abby Lunstrum, Homer Adams, Andrew Harwood, Matthew Schultt, and Julia Mullarney. The summary data used here are available at <http://research.vancouver.wsu.edu/stephen-henderson> and raw data available on request from Stephen Henderson. Funding was provided by National Science Foundation awards 1045286 and 1355211 and by US Geological Survey award 06HQGR0126.

## References

- Atenucci, J. P., J. Imberger, and A. Saggio (2000), Seasonal evolution of the basin-scale internal wave field in a large stratified lake, *Limnol. Oceanogr.*, **45**, 1621–1638.
- Becherer, J., and L. Umlauf (2011), Boundary mixing in lakes: 1. Modeling the effect of shear-induced convection, *J. Geophys. Res.*, **116**, C10017, doi:10.1029/2011JC007119.
- Brink, K. H. (1988), On the effect of bottom friction on internal waves, *Cont. Shelf Res.*, **8**, 397–403.
- Brink, K. H., and J. Allen (1978), On the effect of bottom friction on barotropic motion over the continental shelf, *J. Phys. Oceanogr.*, **8**, 919–922.
- Brink, K. H., and S. Lentz (2010), Buoyancy arrest and bottom Ekman transport. Part II: Oscillating flow, *J. Phys. Oceanogr.*, **40**, 636–655.
- D’Asaro, E. A. (1982), Absorption of internal waves by the benthic boundary layer, *J. Phys. Oceanogr.*, **12**, 323–336.
- Deemer, B. R., S. M. Henderson, and J. A. Harrison (2015), Chemical mixing in the bottom boundary layer of a eutrophic reservoir: The effects of internal seiche on nitrogen dynamics, *Limnol. Oceanogr.*, **60**, 1642–1655.
- de la Fuente, A., K. Shimizu, Y. Nino, and J. Imberger (2010), Nonlinear and weakly nonhydrostatic inviscid evolution of internal gravitational basin-scale waves in a large, deep lake: Lake Constance, *J. Geophys. Res.*, **115**, C12045, doi:10.1029/2009JC005839.
- Freidrichs, C., and L. Wright (1997), Sensitivity of bottom stress and bottom roughness estimates to density stratification, Eckernförde Bay, southern Baltic Sea, *J. Geophys. Res.*, **102**, 5721–5735.
- Fugate, D. C., and R. J. Chant (2005), Near-bottom shear stresses in a small, highly stratified estuary, *J. Geophys. Res.*, **110**, C03022, doi:10.1029/2004JC002563.
- Goudsmit, G.-H., F. Peeters, M. Gloor, and A. Wuest (1997), Boundary mixing versus internal diapycnal mixing in stratified natural waters, *J. Geophys. Res.*, **102**, 27,903–27,914.
- Henderson, S. M., and B. R. Deemer (2012), Vertical propagation of lakewide internal waves, *Geophys. Res. Lett.*, **39**, L06405, doi:10.1029/2011GL050534.
- Holtappels, M., M. M. Kuypers, M. Schlüter, and B. Volker (2011), Measurement and interpretation of solute concentration gradients in the benthic boundary layer, *Limnol. Oceanogr. Methods*, **9**, 1–13.
- Horn, D., J. Imberger, and G. Ivey (2001), The degeneration of large-scale interfacial gravity waves in lakes, *J. Fluid Mech.*, **434**, 181–207.
- Inall, M. E. (2009), Internal wave induced dispersion and mixing on a sloping boundary, *Geophys. Res. Lett.*, **36**, L05604, doi:10.1029/2008GL036849.
- Ivey, G., and J. Imberger (1991), On the nature of turbulence in a stratified fluid, *J. Phys. Oceanogr.*, **21**, 650–658.
- Kaimal, J., Y. Izumi, J. Wyngaard, and O. Cote (1972), Spectral characteristics of surface layer turbulence, *Q. J. R. Meteorol. Soc.*, **98**, 563–589.
- LaZerte, B. D. (1980), The dominating higher order vertical modes of the internal seiche in a small lake, *Limnol. Oceanogr.*, **25**, 846–854.
- Leaman, K., and T. B. Sanford (1975), Vertical energy propagation of internal waves: A vector spectral analysis of profiles, *J. Geophys. Res.*, **80**, 1975–1978.

- Lenschow, D., J. Mann, and L. Kristensen (1994), How long is long enough when measuring fluxes and other turbulent statistics?, *J. Atmos. Oceanic Technol.*, **11**, 661–673.
- Lohrmann, A., B. Hackett, and L. P. Roed (1990), High resolution measurements of turbulence, velocity and stress using pulse-to-pulse coherent sonar, *J. Atmos. Oceanic Technol.*, **7**, 19–37.
- Lorke, A., and A. Wüest (2005), Application of coherent ADCP for turbulence measurements in the bottom boundary layer, *J. Atmos. Oceanic Technol.*, **22**, 1821–1828.
- Lorke, A., L. Umlauf, T. Jonas, and A. Wüest (2002), Dynamics of turbulence in low-speed oscillating bottom-boundary layers of stratified basins, *Environ. Fluid Mech.*, **2**, 291–313.
- Lorke, A., B. Müller, M. Maerki, and A. Wüest (2003), Breathing sediments: The control of diffusive transport across the sedimentwater interface by periodic boundary-layer turbulence, *Limnol. Oceanogr.*, **48**, 2077–2085.
- Lorke, A., F. Peeters, and A. Wüest (2005), Shear-induced convective mixing in bottom boundary layers on slopes, *Limnol. Oceanogr.*, **50**, 1612–1619.
- Lorrai, C., L. Umlauf, J. K. Becherer, A. Lorke, and A. Wüest (2011), Boundary mixing in lakes: 2. Combined effects of shear- and convectively induced turbulence on basin-scale mixing, *J. Geophys. Res.*, **116**, C10018, doi:10.1029/2011JC007121.
- Lu, Y., and R. G. Lueck (1999), Using a broadband adcp in a tidal channel. Part ii: Turbulence, *J. Atmos. Oceanic Technol.*, **16**, 1568–1579.
- Lucas, N., J. Simpson, T. Rippeth, and C. Old (2014), Measuring turbulent dissipation using a tethered adcp, *J. Atmos. Oceanic Technol.*, **31**, 1826–1837.
- Maas, L. R., and J. van Haren (1987), Observations on the vertical structure of tidal and inertial currents in the central North Sea, *J. Mar. Res.*, **45**, 293–318.
- MacIntyre, S., and R. Jellison (2001), Nutrient fluxes from upwelling and enhanced turbulence at the top of the pycnocline in Mono Lake, California, *Hydrobiologia*, **466**, 13–29.
- Mei, C. C. (1989), *The Applied Dynamics of Ocean Surface Waves*, World Sci., N. J.
- Monin, A., and A. Yaglom (1975), *Statistical Fluid Mechanics: Mechanics of Turbulence*, Dover, N. Y.
- Mortimer, C. (1952), Water movements in lakes during summer stratification, *Philos. Trans. R. Soc. London B*, **236**, 355–398.
- Munk, W., and C. Wunsch (1998), Abyssal recipes II: Energetics of tidal and wind mixing, *Deep Sea Res., Part I*, **45**, 1977–2012.
- Münnich, M., A. Wüest, and D. Imboden (1992), Observations of the second vertical mode of the internal seiche in an alpine lake, *Limnol. Oceanogr.*, **37**, 1705–1719.
- Pannard, A., B. E. Beisner, D. F. Bird, J. Braun, D. Planas, and M. Bormans (2011), Recurrent internal waves in a small lake: Potential ecological consequences for metalimnetic phytoplankton populations, *Limnol. Oceanogr. Fluids Environ.*, **1**, 91–109.
- Perlin, A., J. Moum, J. Klymak, M. Levine, T. Boyd, and P. Kosro (2005), A modified law-of-the-wall applied to oceanic bottom boundary layers, *J. Geophys. Res.*, **110**, C10S10, doi:10.1029/2004JC002310.
- Phillips, O. (1977), *The Dynamics of the Upper Ocean*, 2 ed., Cambridge Univ. Press.
- Pierson, D. C., and G. A. Weyhenmeyer (1994), High resolution measurements of sediment resuspension above an accumulation bottom in a stratified lake, *Hydrobiologia*, **284**, 43–57.
- Rinne, H., A. Delany, J. Greenberg, and A. Guenther (2000), A true eddy accumulation system for trace gas fluxes using disjunct eddy sampling method, *J. Geophys. Res.*, **105**, 24,791–25,798.
- Serra, T., L. J. Vidal, X. Casamitjana, M. Soler, and J. Colomer (2007), The role of surface vertical mixing in phytoplankton distribution in a stratified reservoir, *Limnol. Oceanogr.*, **52**, 620–634.
- Shimizu, K., and J. Imberger (2009), Damping mechanisms of internal waves in continuously stratified rotating basins, *J. Fluid Mech.*, **637**, 137–172.
- Simpson, J. H., N. Lucas, B. Powell, and S. C. Maberly (2014), Dissipation and mixing during the onset of stratification in a temperate lake, Windermere, *Limnol. Oceanogr.*, **60**, 29–41.
- Sleath, J. (1984), *Sea Bed Mechanics*, John Wiley.
- Slinn, D. N., and J. J. Riley (1996), Turbulent mixing in the oceanic boundary layer caused by internal wave reflection from sloping terrain, *Dyn. Atmos. Oceans*, **24**, 51–62.
- Sorensen, J., M. Sydor, H. Huls, and M. Costello (2004), Analysis of Lake Superior seiche activity for estimating effects on pollution transport in the St Louis River estuary under extreme conditions, *J. Great Lakes Res.*, **30**, 293–300.
- Spalding, D. (1961), A single formula for the law of the wall, *J. Appl. Mech.*, **28**, 455–458.
- Stillinger, D., K. Helland, and C. van Atta (1983), Experiments on the transition of homogeneous turbulence to internal waves in a stratified fluid, *J. Fluid Mech.*, **131**, 91–122.
- St. Laurent, L., and C. Garrett (2002), The role of internal tides in mixing the deep ocean, *J. Phys. Oceanogr.*, **32**, 2882–2899.
- Trowbridge, J., W. Geyer, M. Bowen, and A. Williams (1999), Near-bottom turbulence measurements in a partially mixed estuary: Turbulent energy balance, velocity structure, and along-channel momentum balance, *J. Phys. Oceanogr.*, **29**, 3056–3072.
- Umlauf, L., and H. Burchard (2011), Diapycnal transport and mixing efficiency in stratified boundary layers near sloping topography, *J. Phys. Oceanogr.*, **41**, 329–345.
- Vermeulen, B., A. Hoitink, and M. Sassi (2011), Coupled ADCPs can yield complete Reynolds stress tensor profiles in geophysical surface flows, *Geophys. Res. Lett.*, **38**, L06406, doi:10.1029/2011GL046684.
- Vidal, J., F. S. J. Rueda, and X. Casamitjana (2008), Forced resonant oscillations as a response to periodic winds in a stratified reservoir, *J. Hydraul. Eng.*, **134**, 416–425.
- Wiles, P. J., T. P. Rippeth, J. H. Simpson, and P. J. Hendricks (2006), A novel technique for measuring the rate of turbulent dissipation in the marine environment, *Geophys. Res. Lett.*, **33**, L21608, doi:10.1029/2006GL027050.
- Wüest, A., and A. Lorke (2003), Small-scale hydrodynamics in lakes, *Annu. Rev. Fluid Mech.*, **35**, 373–412.
- Wüest, A., G. Piepke, and D. C. Van Senden (2000), Turbulent kinetic energy balance as a tool for estimating vertical diffusivity in wind-forced stratified waters, *Limnol. Oceanogr.*, **45**, 1388–1400.